10TH INTERNATIONAL SYMPOSIUM ON PARTICLE IMAGE VELOCIMETRY – PIV13
Delft, The Netherlands, July 1-3, 2013

Light Field Imaging of Turbulent Liquid Sheet Breakup in Air

Barry E. Scharfman, Douglas P. Hart, and Alexandra H. Techet

Department of Mechanical Engineering, MIT, Cambridge, Massachusetts, USA
barryes@mit.edu

ABSTRACT

The atomization of an unsteady turbulent sheet of water in air is analyzed using a combination of light field imaging (LFI) and synthetic aperture (SA) refocusing techniques. This sheet collides with and initially flows along a solid inclined plate, and imaging is performed in the region where breakup and separation from the plate begin. Ligaments and droplets emanate from the sheet and break off due to capillary instabilities. Image volumes consisting of these flow features, as well as segments of the liquid sheet body, are captured using a multiple CCD sensor array consisting of ten cameras arranged in three rows. Synthetic aperture refocusing techniques are applied to the raw camera array images, each with large depths of field, to obtain a stack of post-processed images, with narrow depth of field, where each image in the stack is located on a specific focal plane. Simulations using a dark field imaging modified version of the aforementioned SA method with nine cameras show that it is possible to extract the center coordinates in three dimensions (3D) and radii of spheres found in a scene being imaged. It is also demonstrated that for two camera arrays with the same number of cameras, a circular array with the same radius as the horizontal and vertical distance between cameras in the square array will result in a more accurate reconstruction.

1. INTRODUCTION

A fundamental challenge in experimental fluid mechanics is the accurate spatial and temporal resolution of three-dimensional, multiphase fluid flows. Whether for determining new fluid phenomena, evaluating new designs, or benchmarking computational codes, fully spatially- and time-resolved experimental data is paramount. Given recent advances in camera and imaging technologies, and the growing prevalence of commercially available light field imaging systems, the opportunity for obtaining such data is achievable at a lower cost and with greater resolution and computational savings. Stemming from the computer vision communities, light field imaging (LFI) and synthetic aperture (SA) refocusing techniques have been combined in an emerging method to resolve three-dimensional flow fields over time [1]. This technique is aptly suited for sprays, particle laden and multiphase flows, as well as complex unsteady and turbulent flows.

At the core of light field imaging, a large number of light rays from a scene are collected and subsequently reparameterized based on calibration to produce a 3D image [2]. In practice, one method used by researchers in the imaging community for sampling a large number of rays is to use a camera array [3, 4] or, more recently, a single imaging sensor and a small array of lenslets (lenslet array) in a plenoptic camera [5]. The novelty of the approach used here is the application of the reparameterization methods to 3D spray fields and fluid flows.

In short, light field imaging involves the reparameterization of images captured using an array of cameras, or from a single senor and lenslet array (i.e. a plenoptic camera), to digitally refocus a flow field post-capture. All cameras record a volumetric scene in-focus, and by recombining images in a specific manner, individual focal planes can be isolated in software to form refocused images. Flow features, such as individual droplets, can be located in three-dimensions by refocusing throughout the volume and extracting features on each plane. An implication of the refocusing is the ability to "see through" partial occlusions in the scene. Initial applications by [1] also proved these techniques viable for quantitative flow measurements when combined with 3D particle imaging velocimetry algorithms and special particle identification thresholding. High-speed cameras were used by Belden et al. [6] with similar success for bubbly flows but with significant equipment cost increase. Techet et al. [7] discuss the application of these techniques to the atomization of a turbulent sheet in air as well as other spray flow conditions. Below the turbulent sheet breakup is analyzed using LFI and SA techniques and issues preventing the extraction of complete shape, size, and position information using these techniques are discussed.

Dark field imaging is a technique that relies on indirect illumination of a scene, rather than having light pass through the object being imaged into the camera lens. This method has traditionally been used in microscopy to image lightly colored or translucent subjects. Zsigmondy [8] developed the first ultramicroscope, or darkfield microscope, in 1903. Sipperley and Bachalo [9] discuss an application of dark field imaging to a solid object along with considerations

relevant for imaging spray flows. They utilized lighting surrounding the target and recorded images of it at different positions and focal depths with a single camera to simulate the concept of inserting multiple CMOS sensors into a single multi-focal plane camera. Here, in simulations similar lighting conditions are utilized in a dark field imaging method that relies on the use of the aforementioned camera array and synthetic aperture refocusing techniques. The essentially binary images that are produced allow for simpler image post-processing and the extraction of center coordinates and radii of imaged spheres in 3D. This method is useful for finding droplet or bubble size and location distributions in 3D space over time.

Figure 1 Ten-camera array of Flea 2 model FL2-08S2M/C from Point Grey Research, Inc. CCD cameras, with 50mm Nikkor lenses, typical of those used for the experiments presented herein.

2. PRINCIPLE

To obtain three-dimensional volumetric data sets for spray fields, we implement a planar array of cameras to record the scene from different angles. Synthetic aperture refocusing techniques are applied to the raw camera array images, each with large depths of field, to obtain a stack of post-processed images, with narrow depth of field, where each image in the stack is located on a specific focal plane. In general, the post-processing for synthetic aperture refocusing involves projecting all images onto a focal surface (planar or otherwise) in the scene on which the geometry is known, averaging the projected images to generate one image, and repeating for an arbitrary number of focal planes [1].

The ten-camera array used in the turbulent sheet breakup experiments discussed below is shown in Figure 1. These cameras are typically arranged in a multi-baseline stereo configuration, which view the scene from different viewpoints. The cameras can be placed at arbitrary locations and angles as long as the desired refocused planes (image volume) are in the field of view of each camera. The depth of field of each camera is set large enough such that the entire volume of interest is in focus. Accurate calibration is also critical in the reparameterization and requires advanced auto-calibration algorithms.

The starting point for volume reconstruction is the implementation of the synthetic aperture algorithm to generate refocused images on planes throughout the volume. Thereafter, the actual particle field must be extracted from the refocused images and organized into a volume with quantifiable locations. First, mapping functions must be established between the camera image planes and world coordinates

$$\boldsymbol{u}_j^i = F\left(\boldsymbol{X}_j; p^i\right), \tag{1}$$

where $\boldsymbol{u}_j$ is the 2x1 vector of the j^{th} image point coordinates, $[u_j, v_j]^T$, X_j is the 3x1 vector of the j^{th} world point coordinates, $[X_j, Y_j, Z_j]^T$, p^i is a set of parameters defining the model of the i^{th} camera, and F defines the form of the model. This model allows each image from each of the N cameras in the array to be projected onto k focal planes. $I_{FP_{ki}}$ denotes the image from camera i aligned on the k^{th} focal plane. The resulting refocused SA image, I_{SA_k}, may be generated by averaging each of these images over the number of cameras in the array

$$I_{SA_k} = \frac{1}{N}\sum_{i=1}^{N} I_{FP_{ki}}, \tag{2}$$

where I_{SA_k} is the image from camera i aligned on the k^{th} focal plane and N is the number of cameras [6]. Combining images using this averaging technique is known as additive refocusing. A variant of the additive SA algorithm that can enhance signal-to-noise ratio for well calibrated images is given by the multiplicative refocusing algorithm

$$I_{SA_k} = \prod_{i=1}^{N} \left[(I_{FP_{ki}})^n \right], \tag{3}$$

where n is an exponent between 0 and 1 [6]. This allows for enhancement of the signal-to-noise ratio without letting any camera with an occluded view of an object prevent that object from being refocused, because a small number raised to an exponent between 0 and 1 is non-zero. It has been determined that n in the range $\frac{1}{5} \leq n \leq \frac{1}{3}$ works best for the synthetic aperture refocusing techniques used in the experiments discussed in the next section.

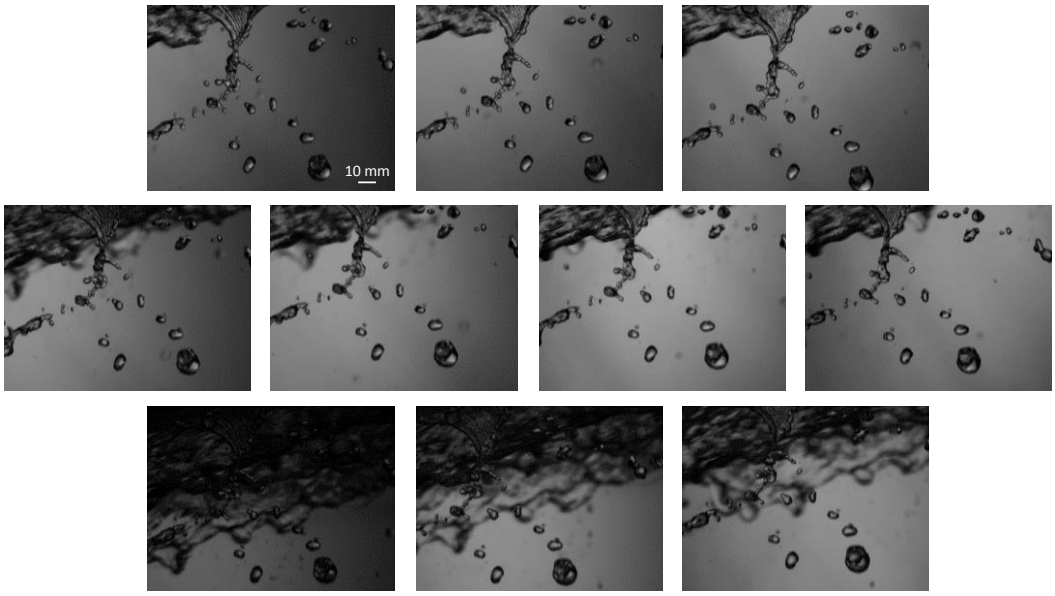

Figure 2 Raw images from individual cameras at a particular instant in time.
Image positions correspond to physical camera positions when looking head-on at the array.

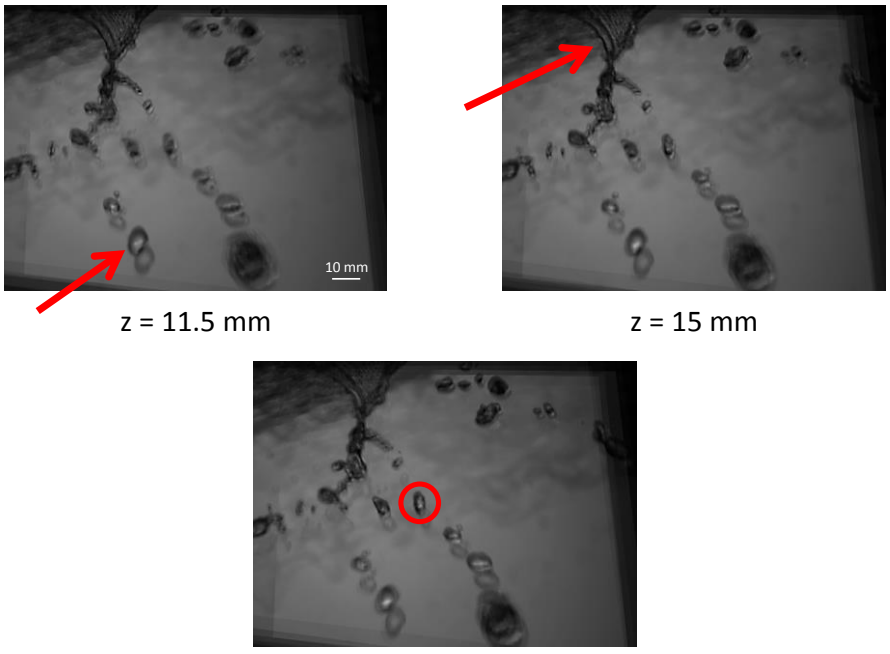

Figure 3 Synthetic aperture refocused images corresponding to the raw images in the previous figure.
The arrows and circle indicate features that are in focus at the particular planes shown.

3. EXPERIMENTS

The experiments described below feature involve the breakup of a turbulent water sheet moving along a solid boundary. For all experiments, the planar camera array in Figure 1 is used. The images are processed using the light field imaging and synthetic aperture refocusing algorithms as described above that were written in MATLAB.

The cameras used in all of the experiments presented herein are Flea 2 model FL2-08S2M/C from Point Grey Research, Inc. All ten cameras in the array were synced and simultaneously captured 1024 x 768 pixels, 8 bit, monochromatic images at 30 frames per second maximum. Although this frame rate was not high enough to achieve fine temporal resolution, it was effective for recording images that could be refocused and from which flow structures, such as droplets and ligaments, could be extracted and investigated. High-speed cameras were used by Belden et al. [6] with similar success but significant cost increase. Each Flea camera is equipped with a Nikon Nikkor 50 mm lens and F-to-C mount adapter. The cameras are arranged in a planar array mounted on 80/20® aluminum rails, in various configurations. All cameras are oriented at angles such they can all record the same image volume simultaneously. The spray is back illuminated by a pulsed LED light bank, which can be synchronized with the camera frame rate; a common light diffuser, such as that used by professional photographers, was used to create uniform, diffuse lighting.

An auto-calibration method relying on a pinhole model was utilized to establish a mapping function between the image planes and world coordinates [10]. For all calibrations, a checkered grid is randomly moved and recorded in different orientations throughout the focal volume for each set of experiments. It is important to make sure that the calibration plate is in focus in every image by each camera in the array to ensure that the auto calibration and refocusing algorithm will succeed in reconstructing the volume.

4. TURBULENT SHEET BREAKUP

The light field imaging and synthetic aperture refocusing techniques are applied to the investigation of the atomization of an unsteady turbulent sheet of water in air. The goal of this project is to characterize the size range and spatial distribution of droplets formed by the unsteady, turbulent atomization of a sheet of water launched into the air at an angle.

A sample set of raw images from each of the ten cameras at a particular time instant is shown in Figure 2. The notable features in these images are the ligaments and droplets of water emanating from the liquid sheet, which is located above the field of view of the cameras in these images. It is interesting to investigate the nature of the shape and size distribution of these structures, which are formed during the primary breakup phase of the sheet atomization. These ten individual camera images are processed using the multiplicative refocusing method with a multiplicative exponent of 1/5 (Eq. 3).

Sample results are shown in Figure 3 at various depths throughout the volume. Features that are in focus at each particular plane in the z (depth) direction are indicated. Negative z values indicate image planes that are in front of the reference plane (closer to the camera array) at the center of the volume of interest, while positive values of z are behind the reference plane. Those structures that are not depicted in sharp focus, or that appear to be ghosting, are actually located at a different depth in the volume and are not in focus on that z-plane. The identification of the plane(s) of focus of particular features allows their positions in the volume to be determined.

Although the location and size of in-focus features in a particular plane of focus can be detected, feature centroids and complete shapes cannot be fully reconstructed using the methods described. The apparent extent of features like droplets and ligaments in the depth direction is larger than the true depth due to the out-of-focus blur. This blur also creates “ghosts” that complicate the extraction of in-focus features at each plane. (However, even if the ghosts are removed, the false depth extent due to blur still exists, as shown below for dark field imaging). In Figure 3, it can be seen that these ghosts are large and often make it impossible to perceive which shapes are actually in focus at a particular depth plane. Ghosts from other features are often also located at the same x-y position as in-focus features in many of the planes, which also cause difficulty in processing the images to find sharp features. This is the case in Figure 3, where the ghosting from the sheet is present in the background of other in-focus droplets and ligaments.

5. DARK FIELD IMAGING

Although it has been demonstrated that it is possible to refocus through the image volume, the experimental data presented thus far reveal several important difficulties in the extraction of three-dimensional flow features. The presence of out-of-focus “ghosts” limits the feasibility of extracting flow features via image processing. While in particle image velocimetry and tracking particles or small flow features it has been shown that it is possible to remove

these artifacts of the blur pattern [1, 6], this removal becomes more challenging when the artifacts are larger and are overlapping. In most cases of the complex sheet breakup, it is impossible to perceive which sections of a particular scene are in focus at each depth. Even for the simple case of an isolated perfectly spherical droplet, the exact shape could not be reconstructed with the particular setup described in the previous section.

Spherical objects can be reconstructed by modifying the lighting setup so that a dark field, rather than a light field, approach is utilized. This method is identical to that described in the previous section, except no light enters the cameras in the array directly. Rather, lights are placed around the scene with a black sheet blocking any light directly opposite the cameras. This results in essentially binary images containing solid white shapes on a black background. Using the multiplicative refocusing method in Eq. 3, the out-of-focus "ghosts" are eliminated. This is because a pixel value of zero for the black background in even one camera image from the array will produce a value of zero for that pixel in the reconstructed volume. As a result, only fully in-focus features appear at each depth slice in the refocused volume as a white, filled-in shape that can be extracted via image analysis. Although this method eliminates shading information, it is beneficial because it simplifies the image analysis.

It is possible to determine the depth of the center of a sphere in 3D by searching for the x-y plane containing the full sphere diameter. Since the diameter can also be measured at that depth, a sphere that matches the measured one can be constructed. The extent of the sphere in the depth direction cannot be extracted directly from the reconstructed volume because of the blur created by the cameras in the array. Increasing the number of cameras would not solve this particular issue. Adding more cameras would only make the blur look more natural but would not allow for accurate depth extent extraction. However, the number of cameras and the relative positions of the cameras in the array do indeed affect the appearance of the sphere in the refocused images. Increasing the number of cameras and using a circular, rather than rectangular, shape of the overall aperture results in improved reconstruction accuracy.

6. SIMULATED SINGLE SPHERE 3D DATA EXTRACTION

The free Blender 3D modeling software package [11] is used to simulate scenes as well as the cameras, lights, and calibration grids to test the dark field imaging SA method. Figure 4 presents a schematic of the position of the camera array, lights, and the black sheet blocking the light from across the cameras used for all of the simulations that follow. The black sheet's center is located at the center of the x-y plane and at a depth of 800 mm. It is square with each side measuring 800 mm and has a thickness of 2 mm all symmetric about its center. Columns of lights 400 mm high with a vertical spacing of 20 mm between lights surround the scene, dark sheet, and the array and are located at a radius of 1 m from the world center and are separated by an angle of 20°. These lights, which are known as lamp objects in Blender, were created such that the light's intensity linearly attenuates to half of its original value at a distance of 2 m from the light's position. Light energy is set at 2000 and environment lighting is turned off except during calibration, when only environment lighting is used and the lamps are removed.

Calibration is performed by rendering a calibration plate similar to that used in the turbulent sheet experiments described above in different coordinates and at various orientations throughout the scene volume. This calibration plate is imaged by each camera in the array, and the resulting simulated photographs are saved as image files for processing. In all that follows, multiplicative refocusing is utilized with an exponent of 1/9 in Eq. 3. However, since the images are essentially binary the exponent value does not matter. Similarly, images of the target simulated scene are rendered for each camera and saved and image files under the dark field imaging lighting condition. Synthetic aperture refocusing algorithms similar to those used to reconstruct the turbulent sheet image volumes are used to process the raw simulated images. Additional algorithms in MATLAB have been written to extract and plot feature locations and sizes in 3D.

Two different camera array configurations were used in the Blender simulations (Figure 5). The coordinates of all nine cameras in both of the arrays are planar. In the first array, the cameras are arranged in a square grid with x and y spacing of 150 mm between cameras. The circular configuration features a central camera surrounded by eight other cameras at a radius of 150 mm, each separated by 45°. All cameras in both configurations are oriented toward the center of the simulated world, which is located at the origin at a z distance of 1 m from the center camera (which has the same coordinates and orientation in both arrays).

To test the dark field imaging SA method and compare the accuracy of the results from the two array configurations, single spheres were plotted at the origin in Blender with radii varying from 4 to 40 mm in increments of 4 mm. These spheres are illuminated using the surround lighting shown in Figure 4 with a black sheet blocking the light across from the cameras. The refocused z depth slice containing the circle of greatest diameter is found, indicating that the center of the sphere is located there. Then the radius is measured using image analysis functions from MATLAB's Image Processing Toolbox. No threshold is applied to the refocused images used for the radii calculations. Depending on the thresholds used, the errors have been found to increase or decrease. All of the spheres are found correctly found to be

located precisely at the origin in the z dimension and very close to the origin in the x and y dimensions.

Figure 6 presents the percent error in the calculation of the spheres' radii using both the square and circular camera arrays. As expected, the error decreases with increasing radius since differences in pixel measurement for the radius become smaller relative to the actual radius value as the sphere radius increases. Due to the small size of the 4 mm sphere, small errors in radius measurement have a larger impact on the error. In all cases except for the 4 mm sphere, the circular array outperforms the square one. This should generally be the case because the relative orientation of the cameras for the circular array results in a more natural blur pattern. In the case of the square array, it is observed that the reconstructed sphere appears more angular in the refocused z depth slices due to the angles and orientations of the cameras in this array. The slices of the sphere look more circular, as they should, for the circular camera array configuration. All percent errors are below 3.5%, with most being below 2%. All of the percent errors for the circular array measurements other than the 4 mm sphere are below 1%. This indicates relatively good agreement between the simulated and measured sphere radii.

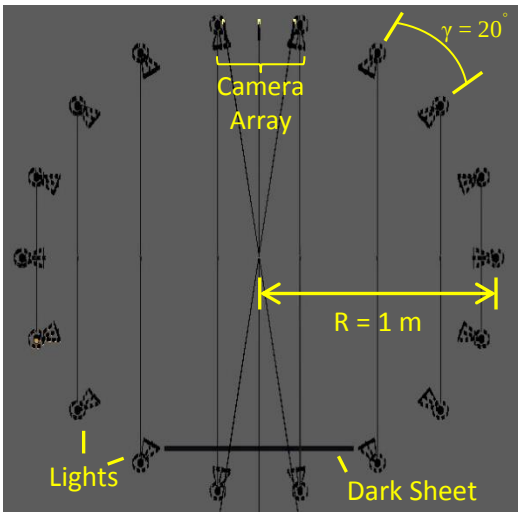

Figure 4 Rendering setup schematic (top view). Lights surround the scene in a circle of radius 1 m. A dark sheet is positioned across from the camera array for the dark field imaging technique.

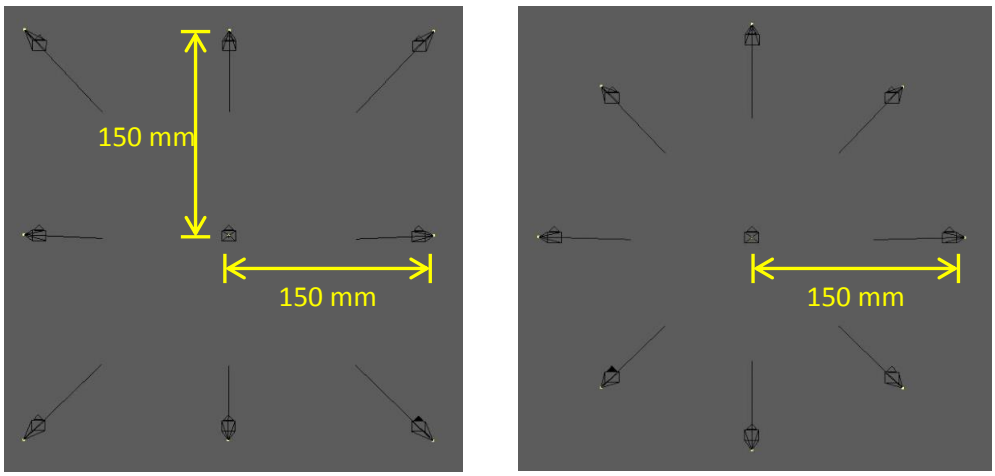

Figure 5 Square (left) and circular (right) camera array orientation schematics (viewed from behind the array looking in the same direction as the center camera). All cameras are located at a depth of z = –1 m relative to the center of the simulated world at the origin.

7. SIMULATED THREE SPHERE OCCLUSION 3D DATA EXTRACTION

In the case of the turbulent sheet atomization and in most other sprays, droplets are often found to occlude each other in images of the spray. Extracting accurate droplet size and location distributions requires a method that can handle such occlusions. To verify that the dark field synthetic aperture technique can be used in such situations, three solid spheres

are rendered using Blender that overlap each other when viewed from various angles, including the z direction. These rendered spheres are shown in the top image in Figure 7. The colors of the spheres are only used as a visual aid for comparison with the plot at the bottom of Figure 7, which shows the same spheres constructed from the refocused images of the rendered spheres.

Figure 8 presents three refocused depth slices for the three spheres from Figure 7. At each depth shown, a different sphere's center is in focus. Scale bars indicate the diameter of the in-focus sphere center at each depth. The circle corresponding to the in-focus sphere center has a larger diameter at the central plane of focus than at any other plane.

The bottom-left two spheres in Figure 8 (which are the green and red spheres on the right in both images in Figure 7), overlap in the refocused image. The centers and radii of these circles are found by calculating the radius of curvature from three points on each circle's circumference. This can be done as long as the circles do not completely overlap when their faces are close enough together in the depth direction. Two circles that are far enough apart in z such that their blur depth extents do not overlap can be distinguished even if they completely overlap in x-y planes.

Table I shows the center coordinates and radii for the three sphere simulation, and Table II presents the error in the calculation of these quantities based on the refocused image volume of the spheres. All coordinate measurements in each dimension have an error less than 0.5 mm. The z coordinates of the spheres were measured exactly by determining the plane containing the largest diameter circle corresponding to a particular sphere, as mentioned above. As expected based on the single sphere simulations, the percent error in radius measurement decreases with increasing sphere radius. The maximum error in any of the radii measurements is less than 4.5%, indicating relatively good agreement between the simulated and measured scene properties. This simulation demonstrates the ability to locate spheres and measure their radii at positions other than the origin, even in the presence of occlusions.

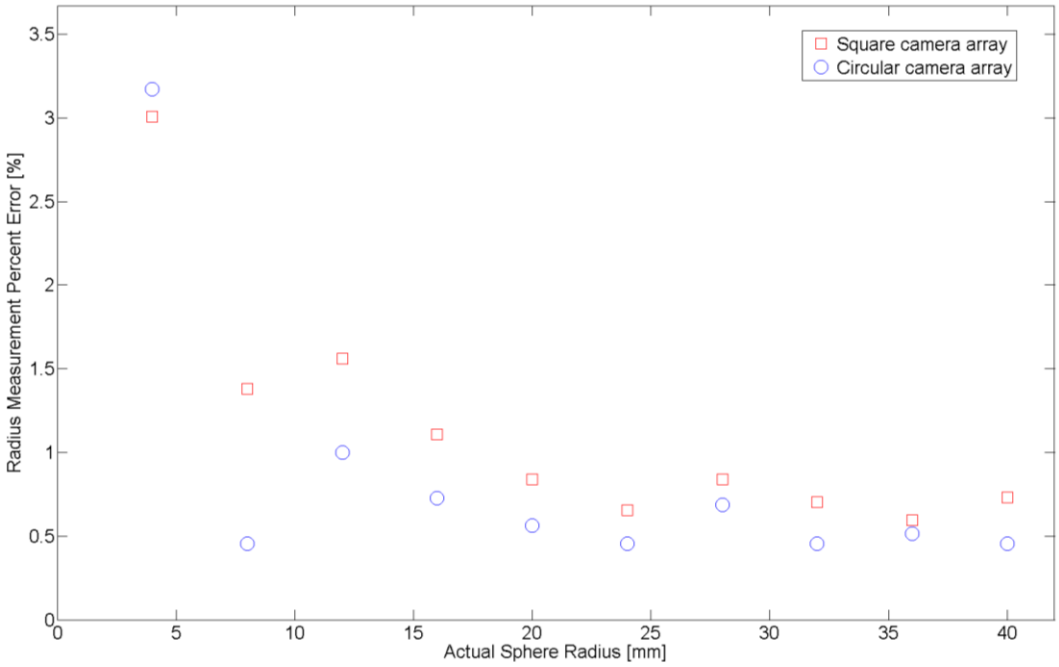

Figure 6 Single sphere error calculations for both the square and circular camera arrays. For each measurement, a single sphere is located at the origin of the simulated world with a radius in the range of 4 to 40 mm in increments of 4 mm.

8. CONCLUSIONS

LFI and SA techniques have been applied to the study of the atomization of an unsteady turbulent sheet of water in air. Ligaments and droplets from the sheet have been imaged, and sharp features are located in 3D. Difficulties with this technique as applied to relatively large features like the ones in this investigation have been identified. Out-of-focus blur prevents accurate depth extent calculation and ghosting complicates the task of image analysis and complete 3D feature extraction.

Simulations using Blender relying on a dark field imaging SA method show that it is possible to extract the center coordinates in three dimensions (3D) and radii of spheres found in a scene being imaged. Renderings of single spheres

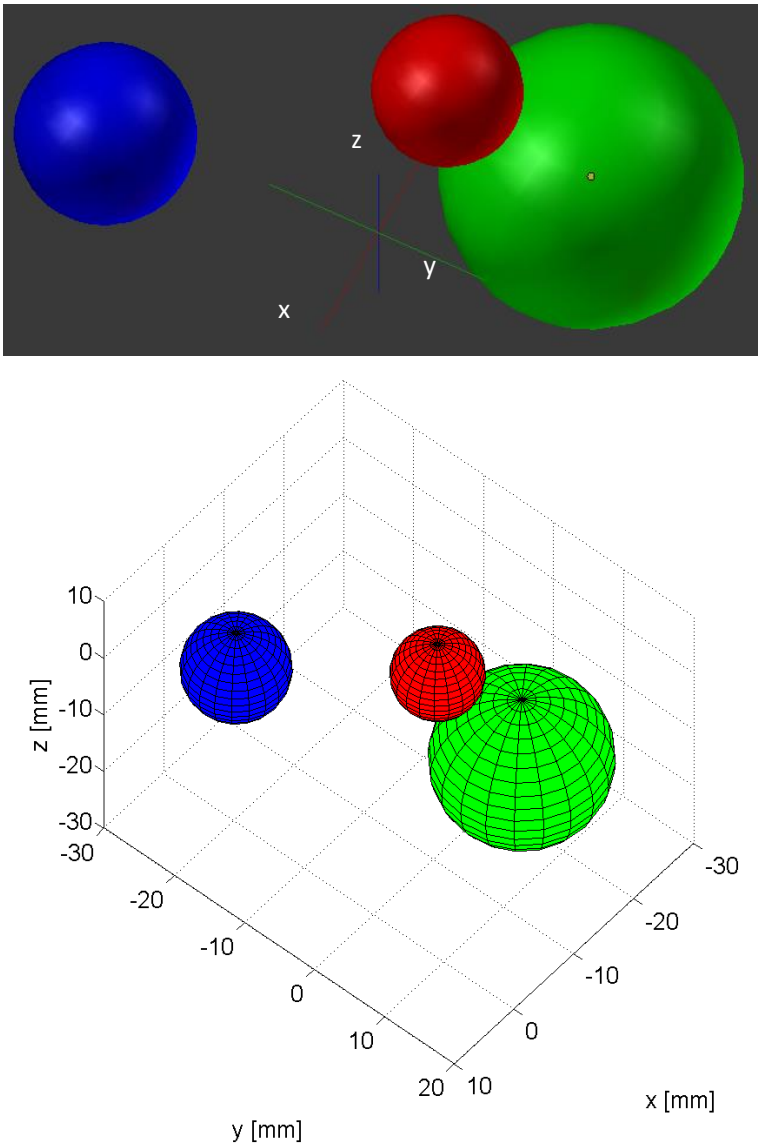

Figure 7 Three sphere rendering (shown on top) and extracted sphere location and radii plot (shown on bottom) using the circular camera array. Sphere colors only serve as a visual aid to match corresponding spheres in the two images.

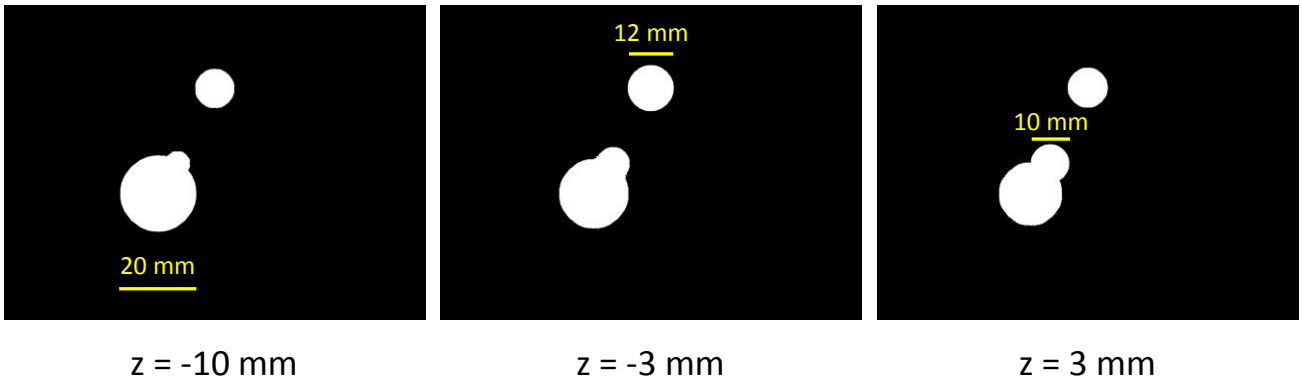

Figure 8 Refocused depth slices for the three sphere rendering shown in Figure 10. At each depth shown, a different sphere's center is in focus. Scale bars indicate the diameter of the in-focus sphere center at each depth. The circle corresponding to the in-focus sphere center has a larger diameter at the central plane of focus than at any other plane.

	Center x Coordinate	Center y Coordinate	Center z Coordinate	Radius
Sphere 1	0	–20	–3	6
Sphere 2	–15	8	–10	10
Sphere 3	–10	0	3	5

Table I Simulated spheres' center coordinates and radius (all units are mm) from the three sphere simulation in Figure 7.

	Center x Coordinate (mm)	Center y Coordinate (mm)	Center z Coordinate (mm)	Radius (%)
Sphere 1	0.019	0.245	0	2.252
Sphere 2	0.071	0.311	0	2.105
Sphere 3	0.046	0.467	0	4.427

Table II Error for extracted spheres' center coordinates (measured as the absolute difference between measured and simulated coordinates in mm) and percent error in the radius from the three sphere simulation in Figure 7.

of varying radii at a single location have been used to demonstrate the ability of the technique to reliably measure sphere size. A simulation involving three spheres with occlusions shows the capability of this method to locate spheres and measure their radii at positions other than the origin, even when spheres partially block each other from view.

ACKNOWLEDGMENTS

The authors would like to thank the Naval Engineering Education Center and the Office of Naval Research (Grant No. N00014-11-1-0545 monitored by Dr. Steven Russell) for funding this work. Abhishek Bajpayee at the MIT Experimental Hydrodynamics Laboratory is acknowledged for his assistance in generating the Blender simulations and updating the synthetic aperture refocusing software that was used to process the simulated photographs.

REFERENCES

[1] Belden J, Truscott TT, Axiak M, Techet AH "Three-dimensional synthetic aperture particle image velocimetry" Meas Sci Technol 21 (2010) pp.1-21

[2] Isaksen A, McMillan L and Gortler SJ "Dynamically reparameterized light field" *SIGGRAPH '00: Proc. 27th Ann. Conf. on Computer Graphics and Interactive Techniques* (New York: ACM Press/Addison-Wesley) (2000) pp. 297–306

[3] Vaish V, Wilburn B, Joshi N and Levoy M "Using plane + parallax for calibrating dense camera arrays" *Proc. 2004 IEEE Computer Society Conf. on Computer Vision and Pattern Recognition (CVPR04') (June–July 2004)* v. 1, (Los Alamitos, CA: IEEE Computer Society Press) (2004) pp. 2–9

[4] Vaish V, Garg G, Talvala E, Antunez E, Wilburn B, Horowitz M, Levoy M "Synthetic aperture focusing using a shear-warp factorization of the viewing transform" *Proc. IEEE Computer Society Conf on Computer Vision and Pattern Recognition (CVPR05')*—June Workshops. Los Alamitos, CA: IEEE Computer Society Press (2005) 3:129

[5] Lynch, K "Development of a 3-D Fluid Velocimetry Technique based on Light Field Imaging" MS Thesis, Auburn University, Auburn, Alabama (2011)

[6] Belden J, Truscott TT, Ravela S, Techet AH "Three-Dimensional Bubble Field Resolution Using Synthetic Aperture Imaging: Application to a Plunging Jet" Exp. Fluids 53 (2012) pp. 839–861

[7] Techet AH, Scharfman BE, Milnes TB, & Hart, DP "Light Field Imaging of Fuel Droplets and Sprays," *Proceedings of the 16th International Symposium on Applications of Laser Techniques to Fluid Mechanics*, Lisbon (2012)

[8] Zsigmondy R and Alexander J "Colloids and the ultramicroscope; a manual of colloid chemistry and ultramicroscopy" New York: John Wiley & Sons (1909)

[9] Sipperley CM and Bachalo WD "Volumetric Imaging and Multi-Angle Illumination for Dense Sprays Characterization" Proceedings of the 25th ILASS Annual Conference on Liquid Atomization and Spray Systems, Pittsburgh, PA (2013)

[10] Belden J, Ravela S, Truscott TT, Techet AH "Three-dimensional synthetic aperture imaging and resolution of multi-phase flows. *Proc ASME-JSME-KSME Joint Fluids Engineering Conf* Hamamatsu, Shizuoka, Japan (2011)

[11] Blender Foundation. http://www.blender.org/. 29 May 2013